Applied Catalysis B: Environmental 113–114 (2012) 201–211

Contents lists available at SciVerse ScienceDirect

Applied Catalysis B: Environmental

journal homepage: www.elsevier.com/locate/apcatb

Aqueous-phase furfural-acetone aldol condensation over basic mixed oxides

Laura Faba, Eva Díaz, Salvador Ordóñez*

Department of Chemical Engineering and Environmental Technology, University of Oviedo (Faculty of Chemistry), JuliánClavería s/n, 33006 Oviedo, Spain

ARTICLE INFO

Article history:
Received 10 August 2011
Received in revised form
21 November 2011
Accepted 24 November 2011
Available online 3 December 2011

Keywords:
Aldol reaction
Basic catalysis
Biomass upgrading
C–C coupling

ABSTRACT

Catalytic aqueous-phase aldol-condensation of acetone and furfural has been studied in this work. Three different mixed-oxides catalysts (Mg–Zr, Mg–Al and Ca–Zr, with different basic sites distribution) were studied, their activity and selectivity being correlated with their physico-chemical properties. Catalysts with the highest concentration of basic sites (especially medium-strength basic sites) are the most active and selective for the C13 fraction, whereas molar ratios of 1:1 yield the highest selectivities for C13 fraction (more than 60% atomic yield for the Mg–Zr mixed oxide). Concerning to reaction mechanism, *cis* isomers are the first ones formed, whereas *trans* isomers are the most abundant at higher reaction times. The main causes of catalysts deactivation are the modification of the physico-chemical properties of catalysts – because of the interaction with water – and in minor extent, the leaching effect; although homogeneous catalytic effects are discarded at studied conditions.

The products formed, and the kinetic dependence on reactant concentration, are consistent with a catalytic mechanism in which the rate-determining step is the formation of the enolate species. The model considers consecutive reversible reactions yielding C8, in the first step, and C13, in the second step; with a first-order dependence on the species with α-hydrogen (acetone and C8), and zero-th order on those species without it (furfural and C13).

1. Introduction

The depletion of fossil fuel reserves and the increasing concern about global climate change have accelerated the development of fuel production pathways based on renewable resources. Although there is a vast amount of renewable sources for electricity generation (wind, solar, etc.), biomass is the only renewable resource allowing the manufacture of liquid fuels for transportation [1]. On the other hand, the so-called first generation biofuels (biodiesel and bioethanol) are industrially obtained from crops (starch and triglyceride containing seeds, fruits or roots) that compete with food purposes. Therefore, the development of new processes using the whole lignocellulosic biomass is of key interest, because these processes allow using many kinds of wastes (switchgrass, sawdust, low-priced woods, crops wastes, municipal wastes, etc.) as raw materials [2].

Transformation of biomass can proceed by different routes involving biological, thermal, enzymatic or chemical processes [3]. Chemical processes are the most flexible ones, being possible to use the cheapest and most abundant forms of biomass (such as low quality cellulose, and hemicelluloses) as raw material [4]. The first step in these chemical methods is the transformation of the biomass into sugar solutions useful for enzymatic and biological transformations (such as bioethanol manufacture). However, the presence of bio-incompatible sugar degradation products, such as furfural, as well as the chemical complexity of these solutions, hinders these upgrading procedures [5]. These furanic compounds (furfural or 5-hydroximethylfurfural), obtained from sugars by catalytic dehydration under mild conditions [6], are valuable chemical platform for manufacturing chemicals and fuels. Direct hydrogenation of these compounds is feasible [7], but it leads to linear C5–C6 hydrocarbons with very poor performance as fuels. However, the aldol condensation of these furanic compounds, or within these compounds and other bioorganic molecules leads to C_{13}–C_{15} adducts, which can be transformed upon hydrogenation and deep hydrodeoxygenation in high-quality diesel fuels. Therefore, Dumesic and co-workers, proposed a process for obtaining these fuels from furfural and acetone involving the three above-mentioned sequential steps [8,9]. Among these steps, the aldol condensation is the step that determines the overall number of carbon atoms and, hence, the resulting quality of the obtained fuel. This reaction was initially carried out by aqueous NaOH solutions, as homogeneous catalyst [5,10], but present several problems such as the difficult recovery or the corrosion.

Heterogeneously catalyzed aldol condensations have been widely studied in the last decades, but essentially in gas phase. However, aqueous phase environment raises new problems, such as different reaction mechanisms [11], enhanced catalyst leaching

* Corresponding author. Tel.: +34 985 103 437; fax: +34 985 103434.
E-mail address: sordonez@uniovi.es (S. Ordóñez).

0926-3373/$ – see front matter © 2011 Elsevier B.V. All rights reserved.
doi:10.1016/j.apcatb.2011.11.039

[12], and solubility problems [9]. Thus, the development of reusable solid catalysts for aqueous reaction having high activity for this reaction, as well as a complete understanding of the reaction mechanism, has generated an increasing interest.

In the present work, the performance of three basic catalysts for the aqueous-phase aldol condensation of acetone and furfural is studied, determining the effect of the reactant concentration and catalyst properties on the condensation efficiency. Reactivity trends were correlated with physico-chemical properties of the materials, proposing a reaction mechanism and a kinetic model for fitting the data. The three selected materials were the Mg–Zr mixed oxide proposed in the works of Dumesic and co-workers [8,9], a mixed oxide obtained from an Al–Mg hydrotalcite, and a Ca–Zr mixed oxide with enhanced basic properties. These materials have been chosen since they have been previously used with promising results in other basic reactions. Mg–Al mixed oxide was used in reactions of aldol condensation of citral and acetone [13], Knoevenagel condensation between glyceraldehyde acetonide and ethyl acetoacetate [14] or isobutyl alcohol obtained by Guerbet condensation of ethanol [15]. Recent reports approach the use of Mg–Zr mixed oxide in processes as the production of biodiesel by transesterification reaction using microalgae oil as raw material [16], Knoevenagel condensation of benzaldehyde and ethyl acetoacetate [17], as well as this aldol condensation [18].

2. Experimental and materials

2.1. Materials

Mg–Al layered double hydroxide (LDH) with Mg/Al ratio of 3 was synthesized by co-precipitation at low super-saturation conditions – constant pH – [19]. The procedure involves the K_2CO_3-assisted precipitation of Mg–Al hydroxide from aqueous nitrate solutions in presence of ultrasonication, the drying of the resulting hydroxides, and their subsequent calcination at 723 K. Further experimental details are given in [19].

Magnesia–zirconia ($MgO–ZrO_2$) catalyst was synthesized using the sol–gel technique proposed by Aramendía et al. [20]. Magnesium nitrate and zirconyl nitrate aqueous solutions were used as precursors, being the preparation procedure fully described in a previous work [21].

Mesoporous $CaO–ZrO_2$ nano-oxide was prepared by a solid–gel route, according to the method described by Liu et al. [22]. One gram of amphiphilicpoly(alkylene oxide) block copolymers ($PEO_{20}PPO_{70}PEO_{20}$, Pluronic P123) (Aldrich) was dissolved in 40.21 mL of absolute ethanol (Panreac, 99.5%). As the surfactant was completely dissolved, 1.01 g of calcium nitrate (Panreac, 99.0%) was added. To this solution, 4.45 g of zirconium(IV) n-propoxide (Aldrich, 70 wt% solution in 1-propanol) mixed with 0.5 g of acetylacetone (acac) (Panreac, 99%) was added with vigorous stirring. Upon stirring at room temperature for 1 h, 1.8 g of deionized water was added drop wise. The mixture was gelled in a closed vessel at 323 K for 24 h. Then, the products were washed with deionized water and filtered. Finally, the sample was heated in flowing He at a ramping rate of 5 K/min to 973 K.

2.2. Experimental and analysis

2.2.1. Catalysts characterization

The crystallographic structures of the mixed oxides were determined by XRD using a Philips PW 1710 diffractometer, working with the Cu-K_α line ($\lambda = 0.154$ nm) in the 2θ range of 5°–85° at a scanning rate of 2θ of 2°/min. The textural characteristics of specific surface area and pore volume were estimated by nitrogen physisorption at 77 K in a Micromeritics ASAP 2020 surface area and porosity analyzer. Physisorption data has been analyzed using BET and BJH approaches for determining surface area and pore volume, respectively.

The strength and distribution of the basic/acid sites were determined by temperature programmed desorption of preadsorbed CO_2 or NH_3 in a Micromeritics TPD/TPR 2900. Samples (10 mg) were treated in He at 723 K for 2.5 h and exposed to a CO_2 or NH_3 (2.5% NH_3 in He) stream at 323 K temperature until saturation coverage was reached. Weakly adsorbed CO_2 or NH_3 was removed by flushing with He at the same temperature for about 1.30 h. The temperature was then increased at a linear rate of 5 K/min from 293 K to 723 K and the rate of CO_2 or NH_3 evolution was monitored by mass spectrometry. The same device has been used for performing TPO analysis of the used catalysts, following CO and CO_2 concentration in the outlet gases.

The nature of basic sites was corroborated by CO_2 chemisorption analyzed by Fourier transform infrared (FTIR) spectroscopy, using a Bruker Vector 22 FTIR spectrophotometer (deuteratedtriglycine sulfate (DTGS) detector), in the 4000–400 cm^{-1} range, with a resolution of 2 cm^{-1} and using 100 scans. The bulk chemical composition of all the samples was determined by ICP-MS, using an octapole HP-7500c. The samples were dissolved in HNO_3 1% (1:250) and Rh was used as internal standard. The surface composition of the mixed oxides was measured by X-ray Photoelectron Spectroscopy (XPS), using a SPECS system equipped with a Hemispherical Phoibos detector operating in a constant pass energy, using Mg–Kα radiation ($h\upsilon = 1253.6$ eV). The samples were fixed to the sample holder using a carbon adhesive tape. The background pressure in the analysis chamber was kept below 4×10^{-9} mbar during data acquisition. Since samples are no-conductors it was needed to use a low energy electron flow gun in order to compensate the charging effects [23]. Correctness of binding energy assignations was checked with the C 1s line.

2.2.2. Reaction studies

Reactions were carried out in a 0.5 L stirred batch autoclave reactor (Autoclave Engineers EZE Seal) equipped with a PID temperature controller and a back pressure regulator. The reactor was loaded with 0.25 L of an aqueous solution of furfural (Panreac, 98%) and acetone (Panreac, 99.5%), resulting aqueous solution with 5 wt.% of organic compounds for the 1:1 ratio. 500 mg of the catalyst was added (with an average particle diameter of 50–80 μm) and air is purged out by adding nitrogen up to 55 bar for three times before starting the condensation reaction. The reactor was pressurized to 10 bar with N_2, heated to reaction temperature, and stirred at 1000 rpm for 24 h [23].

Samples were withdrawn from the sampling port during the condensation reaction, filtered, extracted in ethyl acetate (using a volume relation of 1:1) and analyzed by capillary GC in a Shimadzu GC-2010 equipped with a FID detector, using a 15 m long CP-Sil 5 CB capillary column as stationary phase and quantitative responses were determined using standard calibration mixtures. The calibration samples were prepared with known concentrations of each compound in aqueous phase and carrying out the extraction with the same ratio ethyl acetate/water that was going to be used in the sample analysis. Peak assignment was performed by GC–MS in a HP 6890/5973 instrument, using a 15 m long CP-Sil 5 CB capillary column as stationary phase. The C8 compound was identified checking the mass fractionation in the NIST database and C13 compound was identified comparing the retention time and the mass fractionation of the peaks in the mixture sample and the peaks obtained with commercial standard.

Deactivation studies were carried out by collecting the solution obtained after the first reaction with the catalyst in suspension and subjected it to filtration with a 2 μm mesh. The catalyst thus obtained was used in a new reaction with fresh reagents, keeping

out the same conditions of temperature, reagents concentration, pressure, stirring and organic/catalyst ratio.

Both C8 and C13, products of the condensation reaction, have double bonds and functional groups that can lead to different isomers. The identification of each isomer has been carried out by combining the fractionation of the samples with HPLC and the identification by NMR. The fractionation was carried out using HPLC (Agilent 1200 with an UV–vis detector and an Eclipse XDB C18 column) with a fraction collector. The column used was an Eclipse XDB-C18 and the column oven temperature was held constant at 308 K. Isocratic elution mode was used with the mobile phase of 10% MeOH in H_2O; at a flow rate of 0.7 mL/min. Organic products were detected at wavelengths of 216.8 nm, 221.5 nm and 282.8 nm.

The identification was carried out using NMR (Brukner AV600) programmed with an H frequency of 600.15 Hz and C frequency of 150.91 Hz. The samples were dissolved in deuterated chloroform after undergoing 24 h of drying at 378 K. The spectrums obtained were checked with the theoretical values of chemical shift (allows the identification of the product) and J-coupling (determines the optical isomer). The characteristics ^{1}H-RMN and ^{13}C-RMN profiles of the detected products are shown in the Supporting Information.

Metal lixiviation was quantified by ICP-MS, using an octapole HP-7500c. Samples were previously treated with an aqueous HCl/HNO_3 solution (1:30), Rh being used as an internal standard. Formation of carbonaceous deposits was determined by TPO analysis of the used catalysts. The analyses were performed in a Micromeritics TPD/TPR 2900. Spent catalysts (10 mg) were treated in He at 723 K for 2.5 h and exposed to an O_2 (2% O_2 in He) stream while the temperature was increased until 1023 K with a rate of 2.5 K/min.

2.3. Calculations

The extent of the different reactions has been analyzed in terms of reactant conversion. In order to quantify the selectivity for the formation of C_8 and C_{13} condensation products, atomic yield for each of these condensation products has been used. This parameter is defined as carbon atoms in each product considered (C8 or C13) divided by acetone and furfural atoms in the feed, as it is shown in the Eqs. (1) and (2):

$$\psi_{C8}\% = \frac{8 \cdot \text{mol C8}}{5 \cdot \text{mol C5}_{t=0} + 3 \cdot \text{mol C3}_{t=0}} \cdot 100 \quad (1)$$

$$\psi_{C13}\% = \frac{13 \cdot \text{mol C13}}{5 \cdot \text{mol C5}_{t=0} + 3 \cdot \text{mol C3}_{t=0}} \cdot 100 \quad (2)$$

Carbon balance parameter was used in order to detect the presence of side effects and unconsidered reactions. It was calculated as carbon atoms analyzed in each sample (C3, C5, C8 and C13) divided by initial carbon atoms (C3 and C5 fed). All the plots and tables are done according to these parameters.

$$\text{C balance}\% = \frac{3 \cdot \text{mol C3} + 5 \cdot \text{mol C5} + 8 \cdot \text{mol C8} + 13 \cdot \text{mol C13}}{3 \cdot \text{mol C3}_{t=0} + 5 \cdot \text{mol C5}_{t=0}} \quad (3)$$

Kinetic data has been fitted to power-law kinetic expressions using the Scientist software. Differential equations for the consumption/formation of reactants/products were set considering batch reactor.

3. Results and discussion

3.1. Catalyst characterization

XRD diffraction patterns of the three catalysts used in this work show similar trends to those reported in the literature (Fig. 1).

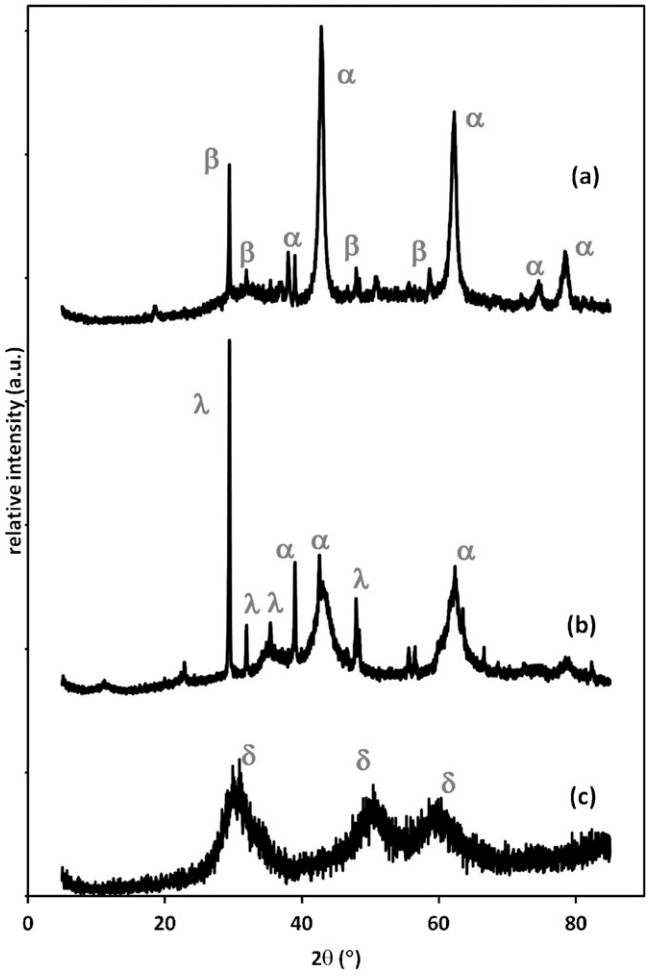

Fig. 1. X-ray diffraction patterns for: (a): MgO–ZrO_2, (b): MgO–Al_2O_3, (c): CaO–ZrO_2. "α" indicates the periclase phases (MgO); "β", ZrO_2 cubic phases; "λ", theta-Al_2O_3 phases; and "δ", ZrO_2 tetragonal phases.

In the case of Mg–Zr mixed oxide, both periclase MgO, JCPDS 00-001-1235, ($2\theta = 43^\circ$, 62°, 74° and 78°) and tetragonal ZrO_2, JCPDS 00-042-1167, ($2\theta = 30^\circ$, 32°, 39°, 48° and 59°) were clearly appreciated [24]. The small peak observed at $2\theta = 38^\circ$ corresponds with brucite ($Mg(OH)_2$), JCPDS00-002-1092, which can be related with an incomplete calcination. In the hydrotalcite-derived Mg–Al mixed oxide, periclase MgO ($2\theta = 29^\circ$, 39°, 43° and 62°) and theta-Al_2O_3, JCPDS 01-086-1410, ($2\theta = 32^\circ$, 35°, 48° and 67°) [25] were the only crystalline phases observed. In the case of Ca–Zr mixed oxide, a very amorphous material is observed (in good agreement with the used preparation process), being only observed width peaks corresponding to cubic ZrO_2 (JCPDS00-027-0997).

The main morphological parameters (obtained by nitrogen physisorption and using the BET and BJH approaches for estimating surface area and pore volume, respectively) are summarized in Table 1, whereas pore size distribution plots are reported in the Supplementary Information. All the tested materials present a markedly mesoporous character. The isotherms of nitrogen adsorption at 77 K showed a noticeable hysteresis at high p/p_0, indicating that the three oxides correspond to type IV materials.

The surface concentration of basic sites, as well as their strength distribution, has been determined by CO_2-TPD. In order to quantitatively compare the differences and similarities among the CO_2-TPD patterns of the different solids, experimental curves were analyzed by a mathematical fitting program and deconvoluted into Gaussian functions (Fig. 2). According to León et al. [19], CO_2

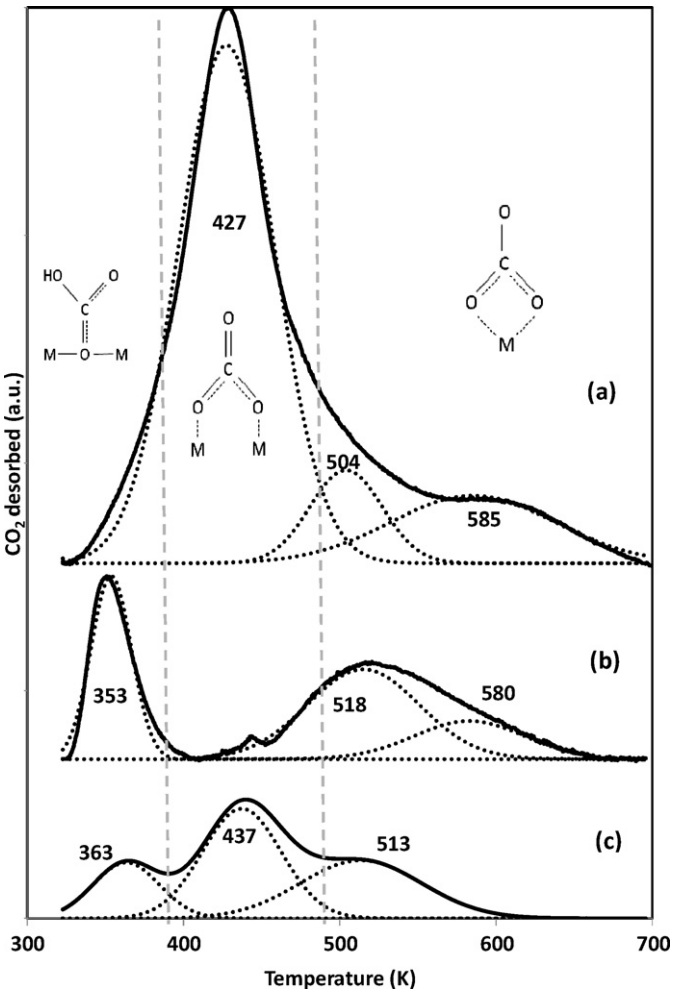

Fig. 2. Deconvolution analysis results of the CO_2-TPD spectra: (a) MgO–ZrO_2, (b) MgO–Al_2O_3, (c) CaO–ZrO_2.

adsorption and subsequent desorption induces the formation of different species from the presence of sites with different basic strengths: bicarbonates (which require surface hydroxyl groups, weak base sites); bidentate carbonates (bridged and chelating, M^{m+}–O^{2-} pairs, medium-strength base sites) or monodentates (O^{2-}, strong base sites). Relating these types of species with the desorption temperature, it was obtained that base centers associated with bicarbonates correspond with 293–373 K, bridged bidentate carbonate with 373–473 K, chelating bidentate carbonate with 473–573 K and unidentate carbonate with temperatures over 573 K [26]. Based on these values, the TPD profiles were deconvoluted in three desorption bands to quantify the density of weak, medium and strong basic sites. The results are presented in Table 1, whereas the IR profiles at different temperatures and a deconvolution example were presented in the supporting information (Figs. S2 and S3, respectively). The evolution of the basic center density is the following: Mg–Zr > Mg–Al > Ca–Zr.

Regarding to their distribution, in all cases the highest proportion is situated in the temperature range 400–520 K, corresponding to carbonate bidentate modes. In Mg–Zr, the first and highest peak corresponds with bridge bidentate centers, and the peak at 504 K to chelating type. Mg–Al only presents chelating type centers, but it has another peak in the range of bicarbonate centers (353 K). Finally, Ca–Zr presents, with much less density, centers type bicarbonate (363 K), bidentate bridge (437 K) and bidentate chelating (513 K). Mg–Zr and Mg–Al presented another significant density around 580 K, that could be corresponded to stronger centers (monodentates). This distribution was corroborated by FTIR, analyzing the strength of the basic sites by CO_2 desorption at 373, 473, 573 and 673 K. The temperature ranges obtained for each type of centers were as expected and consistent with the TPD results.

Measured isoelectric point are in a good agreement with CO_2-TPD observation, being the Ca–Zr mixed oxide the material showing the lowest value (8.8), followed by the Mg–Al (13.1) and the Mg–Zr mixed oxide (11.3). Chemical analysis of the samples was done in order to discard the presence of Na^+ entrapped in the solid that could be responsible of leachable basicity in water. The surface composition and the strength of oxygenated groups were analyzed by XPS and the results are listened in Table 1. The position of O 1s peak is related with its strength when the solid structure is crystalline; in such a way that higher binding energy implies lower basicity [27–29]. The values obtained were 529.0 eV for Mg–Zr, 530.0 eV for Mg–Al and 528.0 eV for Ca–Zr. Thus, the basic sites of Mg–Zr oxide are stronger than for Mg–Al, in agreement with the TPD-CO_2 results. However, this parameter cannot be used to analyze Ca–Zr, due to its amorphous structure.

Acid properties of solid catalysts were analyzed by NH_3-TPD. Results are presented in Table 1 – see profiles in Fig. 3. According to Arena et al. [30], desorption peaks with maximum in the range 473–603 K and 653–773 K are currently attributed to NH_3 chemisorbed on medium and strong acid sites, respectively, being yet not possible to discriminate between Brønsted and Lewis acidity. Peaks with desorption maximum lower than 400 K are associated with NH_3 physisorbed [31]. The three catalysts exhibit their main desorption peaks in the range of strong acid sites, associated with the presence of M^+. These types of centers are related with the acid–basic pairs existed in these catalysts, mainly in Mg–Zr

Table 1
Summary of the main morphological and chemical (from XPS and TPD of NH_3 and CO_2) properties of the catalysts used in this work.

Catalysts	Morphological properties			Base sites (CO_2-TPD)		XPS results		Acid sites (NH_3-TPD)	
	S_{BET} (m^2/g)	D_p (Å)	V_p[a] (cm^3/g)	Strength type	Density (μmol/m^2)	Surface atomic ratio	O 1s binding energy (eV)	Strength type	Density (μmol/m^2)
MgO–ZrO_2	78	342	0.80	Bidentate (427, 504 K)	1.54	11.7 (Mg/Zr)	529.0	Physisorbed (353 K)	62.3
				Monodentate (585 K)	0.17			Lewis acid (500, 566 K)	73.6
MgO–Al_2O_3	168	235	1.09	Bicarbonate (353 K)	0.35	1.6 (Mg/Al)	530.0	Lewis acid (500, 566 K)	13.9
				Bidentate (518 K)	0.47				
				Monodentate (580 K)	0.19			Stronger acid (766 K)	2.1
CaO–ZrO_2	156	57	0.25	Bicarbonate (363 K)	0.04	1.30 (Ca/Zr)	528.0	Physisorbed (473 K)	0.30
				Bidentate (437, 513 K)	0.18			Lewis acid (610 K)	0.80

[a] Estimated according to the method of Barrett, Joyner and Halenda (BJH). Pore volume distributions are provided in the Supporting Information.

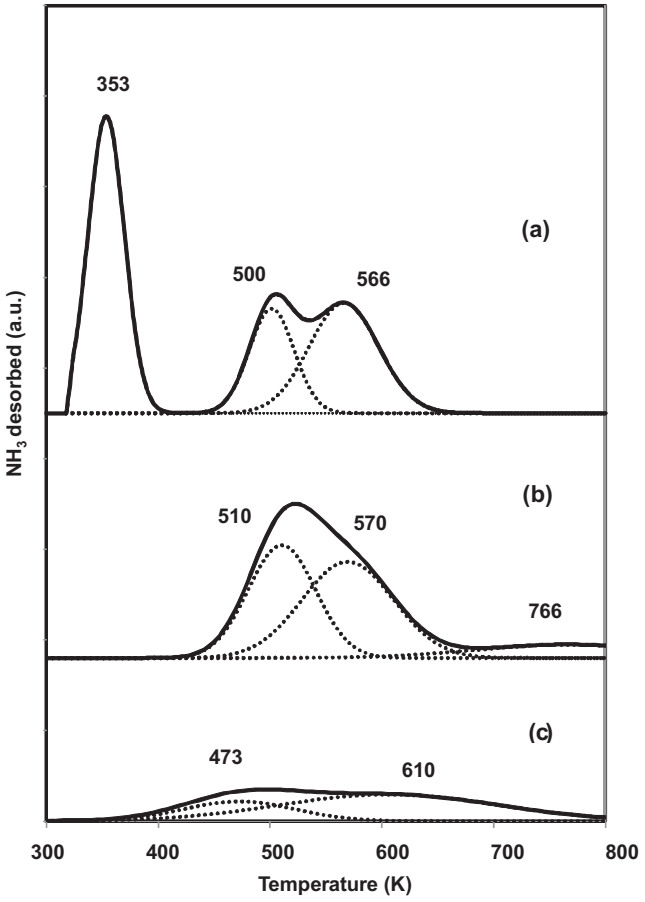

Fig. 3. Deconvolution analysis results of the NH_3-TPD spectra: (a) $MgO–ZrO_2$, (b) $MgO–Al_2O_3$, (c) $CaO–ZrO_2$.

and Mg–Al. The order of density is consistent with the order of basic density which denoted a relationship between both sites. $MgO–ZrO_2$ also exhibits a desorption peak in the range of NH_3 physisorption which is not related with the catalytic activity.

3.2. Reaction studies

Different batch experiments, changing the molar ratio between both reactants, and the catalysts were performed. Fig. 4 shows typical temporal profile of reactants and reaction products for the three studied catalysts. Displayed data correspond to both experiments performed in excess of furfural and excess of acetone, in comparison to the stoichiometric ratios needed for obtaining the C13 adduct (C5/C3 = 2). In general terms, concentration profiles indicate that the reaction follows reversible consecutive reactions (Scheme 1). The only detected side reaction was the acetone condensation for yielding C6 compounds, but less than 10% of the acetone follows this reaction pathway after 24 h reaction time. Therefore, this reaction has not been included in the main discussions.

Acetone reacts with furfural yielding the C8 adduct, which undergoes a subsequent reaction with furfural yielding the C13 product [9,10]. As it could be observed in Fig. 4, Mg–Zr is the most active catalyst in terms of C13 formation, in bothfurfural and acetone excess conditions. In the last conditions, it was denoted that, after 60 h, the C13 concentration remained constant, despite there were enough C5 and C8 to continue the dimer formation. This fact is in agreement with the existence of the retro–aldol condensation, consistent with a balance between C5, C8 and C13 concentrations.

In order to gain further understanding on the reaction mechanism, ^{1}H-RMN of the reaction products after fractionation in a HPLC column was performed. The different isomers found are identified in Fig. 5. Concerning to the C8, this fraction corresponds to a mixture of two different isomers of furfurildeneacetone (same chemical shifts). However, the values of the J-coupling constant are different (13.6, corresponding to the *trans* isomer; and 10 for the *cis* isomer). These values were compared with those obtained with the

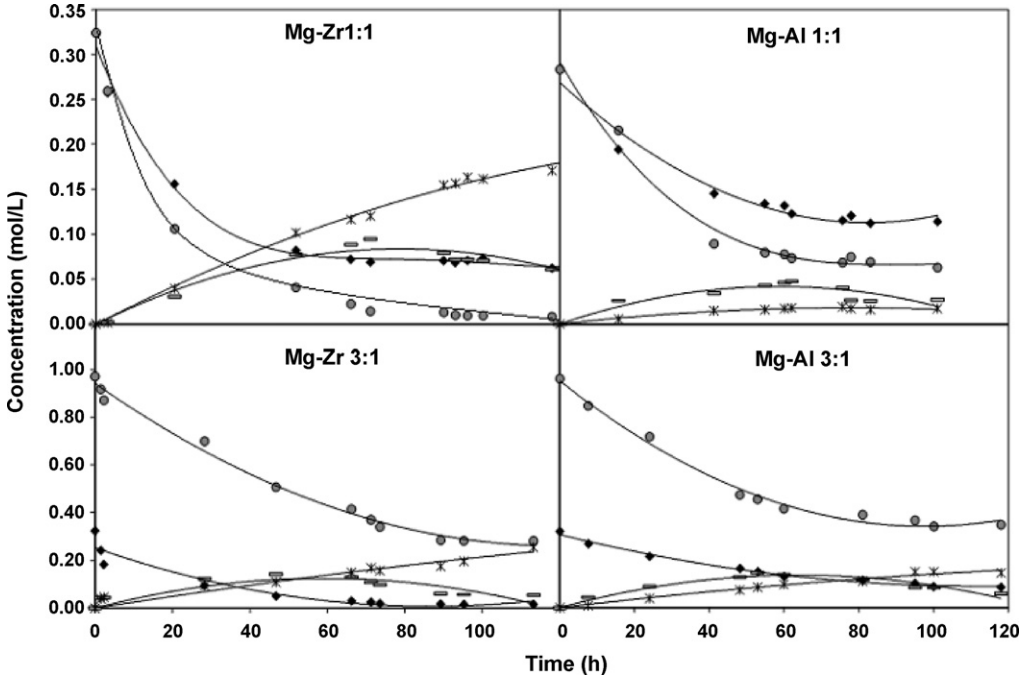

Fig. 4. Concentration profiles of reactants and products in the aldol condensation reaction at 323 K with 1:1 and 3:1 reagents molar ratio, using $MgO–ZrO_2$ and $MgO–Al_2O_3$ as catalysts. Symbols: C3 (♦); C5 (•), C8 (-); and C13 (*).

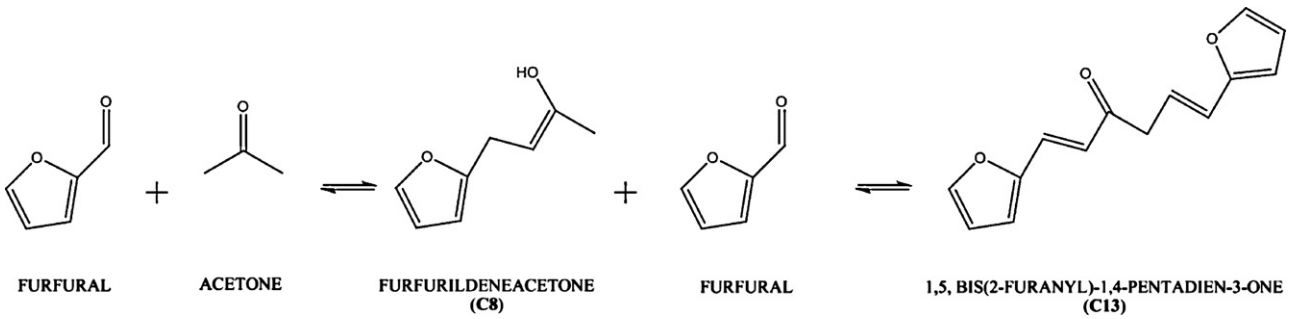

Scheme 1. Reaction network for aldol-condensation of furfural and acetone.

ChemDraw software. Analyzing their evolution with the time, it was obtained the same trend for the three tested catalysts. In a first moment, the reaction advances to the formation of *cis* isomer (initial *cis*/*trans* ratio around 70/30) but after 100 min the trans isomer begins to be the main product: more than a 70% in the case of Mg–Al reaction, and near 95% when Mg–Zr or Ca–Zr are used as catalyst.

Concerning to the C13 fraction, three different isomers of the furfural-acetone-furfural condensation product depicted in Scheme 1 were found based on the different values of the J-coupling constant: *trans–trans* (13.6), *cis–trans* (10 and 13.6) and *cis–cis* isomers (10). The evolution with time follows the same behavior as the monomer (C8). *Cis–cis* isomer was first formed in a higher concentration, with more than 70% in all the cases; whereas after two hours the *trans–trans* isomer came on more than 50%, reaching to more than 90% at the end of the reaction with the three mixed oxides. The *cis–trans* isomer is an unstable form, an intermediate in the C13 isomerization reaction, which has a constant concentration around 5% of C13 in all cases.

In order to check the presence of the reverse reaction, separate experiments were performed with the most active catalyst (Mg–Zr) at the above-mentioned conditions, but feeding aqueous solutions of C8 (4-(2-*furyl*)-3-*buten*-2-*one*, *cis* + *trans*, 98%, Alfa Aesar) or C13 (1,5-*bis*-(2-*furanyl*)-1,4-*pentadien*-3-*one*, 98%, Acros Organics), feeding 3 g in 250 mL. In the case of C13, it was not possible to dissolve all the solid, so the feed was an aqueous suspension. If decomposition reaction occurred, the depletion of C13 in solution (in order to form C8 and C5) would involve the re-dissolution of more C13 to restore the solubility equilibrium. When C8 is used as the only reactant, a C13 selectivity of 8% was obtained after 24 h; which implies that C8 was first decomposed in C5 and C3 (retroaldolization), and the C5 reacted with the excess of monomer (C8) yielding the C13 compound. Accordingly, acetone was also found in this experiment. When the reagent was the C13, a C8 selectivity of 3% was detected after 24 h, as well as 0.8% of furfural. These results suggest a significant contribution of the reverse reactions in both steps, monomer and dimer formation.

The performance of the three studied materials is compared on terms of reactant conversion, atomic yield of the different fractions, and carbon balance closures. The results obtained after 24 h at 325 K and a molar acetone/furfural molar ratio of 1 (the most commonly reported molar ration used in the literature [7–10]), are given in Fig. 6. Comparing C8 and C13 yields, it is observed that the Mg–Zr oxide presents the best performance with values over 60% for C13, followed by the Mg–Al (43%) and Ca–Zr (15.5%). Considering both products, Mg–Al and Mg–Zr got to similar yields (more than 74%). However, C8 formation is more favorable on Mg–Al oxide, due to a higher influence of retro–aldolization reaction. Furthermore, this retro–aldolization reaction is especially important in the C13 formation: C13/C8 ratio obtained for Mg–Al (1.4) contrast with C13/C8 ratio on Mg–Zr oxide (4.2). The carbon balance was in both cases close to 100%, which implies that there were no important secondary reactions. The results obtained in the reaction with Ca–Zr denoted a different behavior: the highest C5 conversion, but a low C3 conversion and C13 yield. These results can be justified since the retro–aldol condensation is also important in the dimer formation, as well as the possible presence of secondary reactions to form heavier products not analyzed. The carbon balance was, according with this fact, being only 75%.

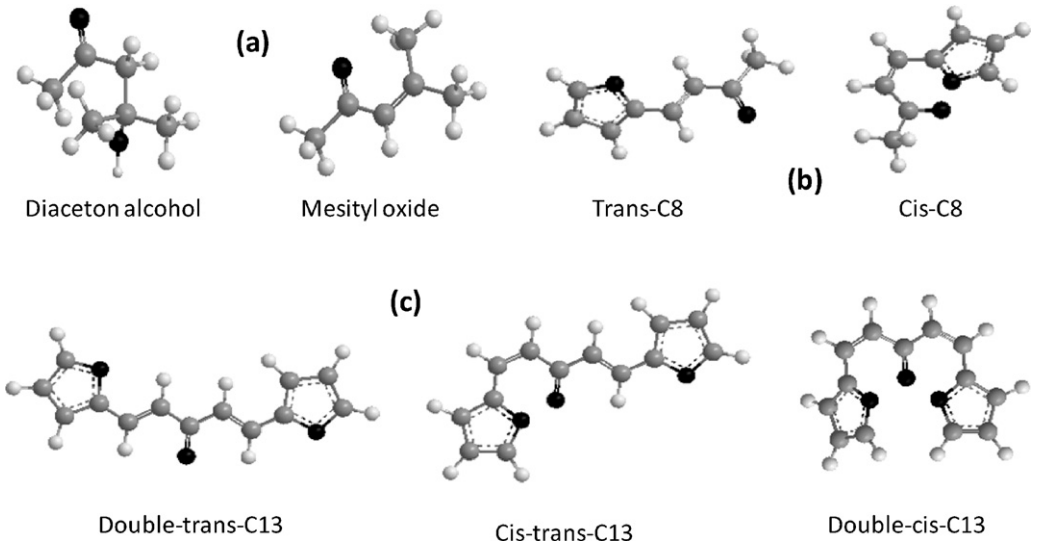

Fig. 5. Isomers identified of C6 (a); C8 (b) and C13 (c) products.

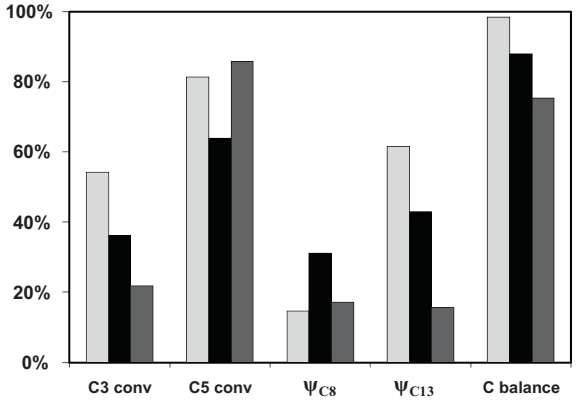

Fig. 6. Results obtained after 24 h reaction time with the three studied catalysts. Grey series bars MgO–ZrO_2, black bars MgO–Al_2O_3; and dark grey bars CaO–ZrO_2.

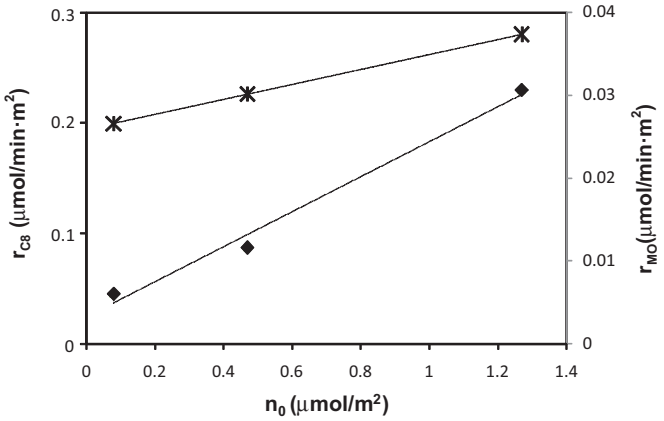

Fig. 7. Initial formation rates on MgO–ZrO_2, MgO–Al_2O_3 and CaO–ZrO_2 catalysts as function of medium-strength base site density (n_0) of C8 (♦) or DAA (*).

Results obtained were also analyzed according to the parameters proposed in the initial studies of this reaction carried on by Huber and Dumesic [7,8], which define selectivities based on the sum of C5, C8 and C13 fractions. No significant differences were found between both methods. With Mg–Zr less than 10% of furfural was detected in the final solution, whereas with Mg–Al and Ca–Zr it was found 30%. Using this calculation basis the differences in C8 selectivity were very light with values between 26% (Mg–Al) and 34% (Ca–Zr). Concerning to C13, the results were very similar than those obtained with the first method.

Activity results can be related to the physico-chemical surface properties of the different catalysts analyzed by different techniques in the characterization, specially the basicity, since aldol condensation is promoted by basic catalysts [26]. Concerning to the BET results, a high surface area seems not be the key parameter that determines the catalytic activity of these oxides. Although the Ca–Zr mixed oxide presents the lowest conversions and selectivities, it seems to be more related to its lower basicity, rather than to diffusional limitations of its porous structure.

According to CO_2-TPD, in this reaction base centers type bidentate carbonate are the most influential. This type of base centers implies the presence of an associated acid site, in this case with medium strength (Lewis type) that participates in the global reaction stabilizing intermediate compounds. Results are in a good agreement with the strength of the basic sites, especially considering the medium strength basic sites (order of reactivity: Mg–Zr > Mg–Al > Ca–Zr). In order to check this correlation, the catalyst activity was compared with the base site densities of each catalyst used. Thus, it was determined the initial C8 conversion rate on an area basis (μmol/min m^2) by calculating the initial slopes in conversions evolution according to:

$$r_{C8}^0 = \frac{1}{S_G} \cdot \left[\frac{dx_{C5}}{d(tW/n_{C5}^0)} \right]_{(tW/n_{C5}^0)=0} \quad (4)$$

where S_G is the surface area (m^2/g), X_{C5} is the C5 conversion, t is the reaction time (min), W is the catalyst weight (g), and n_{C5}^0 is the initial mol of C5. It was obtained a good correlation between the initial C8 formation rate and the density of medium-strength base sites, as shown in Fig. 7. In contrast, a poor correlation was found when this velocity was plotted versus the density of weak or strong basic sites. In this figure, it can also be observed the good correlation between the initial DAA (diaceton alcohol) formation and the density of medium-strength base sites (calculated using a similar procedure as in the C initial rate). These results indicate that under initial conditions, the rate-determining step for both, C8 and DAA formation are promoted by medium-strength base sites.

Fig. 8 shows the influence of the molar ratio of reactants. Five different molar ratios have been studied, from excess furfural to excess acetone, specifically: 3:1, 2:1, 1:1, 1:2 and 1:3 (furfural:acetone, corresponding 2:1 to the stoichiometric ratio needed for C13 formation). For the Mg–Zr oxide (Fig. 8a), a good carbon balance closure is observed, although this closure is lower in acetone excess (because of acetone self-condensations). An excess of acetone produces a noticeable decrease in the dimer selectivity (8% C13 yield in 3:1 conditions, 15% in 2:1), in agreement with the furfural depletion.

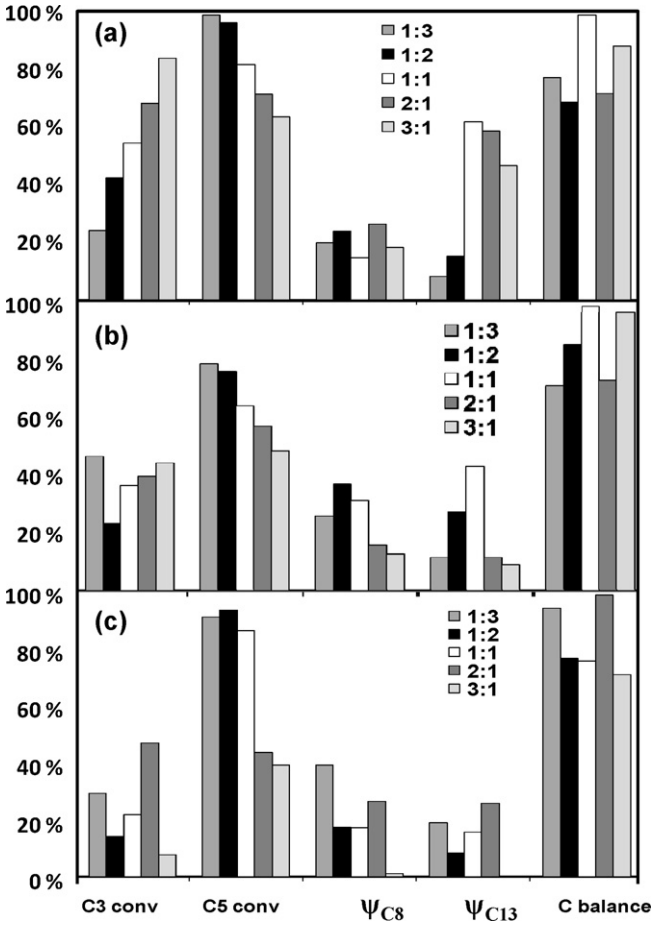

Fig. 8. Results obtained after 24 h of aldol condensation with: (a) MgO–ZrO_2, (b) MgO–Al_2O_3, and (c) CaO–ZrO_2, studying different molar ratios of the reagents (ffl:ace).

Table 2
Comparison of the results obtained after 24 h on stream with the fresh catalysts and the reused catalyst. The aldol condensation was carried out at 323 K with 1:1 (ffl:ace) reactant molar ratio.

		C3 conversion	C5 conversion	ψ_{C8}	ψ_{C13}	C balance
$MgO–ZrO_2$	Fresh catalyst	54.2%	81.4%	14.7%	61.5%	98.4%
	Used catalyst	64.3%	68.0%	11.9%	2.9%	46.1%
$MgO–Al_2O_3$	Fresh catalyst	36.2%	63.8%	31.1%	42.9%	97.8%
	Used catalyst	56.5%	70.8%	3.4%	0.6%	47.4%

Contrary, furfural excess conditions produce a higher selectivity to dimer product, but lower conversion of furfural caused by the depletion of acetone. It is also noticeable, that C13 yield is higher at 1:1 furfural:acetone ratio, although the stoichiometric ratio for C13 formation is 2:1. Considering both products, 1:1 and 2:1 conditions produce almost the same yields (difference lower than 10%), being more favorable the furfural excess (76% total product yield versus 84%, in 1:1 and 2:1 conditions, respectively).

Mg–Al profiles (Fig. 8b) were similar, considering that conversions are lower and, consequently, the product yields too. In this case, an excess of furfural does not imply an increase in the C8 or C13 yield; thus, a stronger influence of reverse reactions in both steps, monomer and dimer formation, is evidenced. Due to this reason, C3 conversion releases almost constant at these conditions. For C13 best results were obtained at 1:1 conditions but, in global terms, condensation products selectivities (C8 + C13) were very similar in 1:1 or 1:2 conditions (less than 10% difference).

Fig. 8c shows the profile obtained using Ca–Zr oxide as catalyst. In this case, the trend was less clear, especially for the C13 selectivity. With this oxide, 2:1 conditions implied the higher C13 selectivity (26%), but results were very similar with acetone excess (19%). Moreover, C8 selectivity increased considerably at these conditions and the carbon balance shows that secondary reactions were no relevant.

3.3. Catalyst stability

In general terms, two different deactivation causes are reported in these catalytic reactions: fouling caused by subsequent aldol condensations, and leaching of active compounds from the catalyst in the aqueous medium.

In order to check the importance of these carbonaceous deposits, TPOs of the used catalysts have been performed, Fig. SI4. In general, similar profiles were observed for Mg–Zr and Mg–Al catalysts (catalysts with highest carbon balance closures): a single asymmetric peak at 700–750 K. This peak can be deconvoluted into two symmetric peaks. Separate experiments performed saturating the catalyst with aqueous solutions of C8 and C13 adducts at room temperatures allow associating the first peak to the adsorption of C8 species and the second one to the adsorption of C13. In good agreement with the reported selectivities, C13 peak is highest for Mg–Zr mixed oxide. By contrast, these peaks are not observed in the case of the Ca–Zr mixed oxide (the catalyst showing worst carbon mass balance closures), which shows a very broad combustion peak centered at higher temperatures. This fact, as well as the poor carbon balance closure, suggests that Ca–Zr mixed oxide catalyzes undesired condensation reactions, leading to the formation of carbonaceous deposits and low selectivity for the desired C8 and C13 adducts. This behavior is related to the lower concentration of basic sites in this material, decreasing the selectivity for the condensation reaction, whereas side reaction are more likely to take place because of the higher surface concentration of reactants.

The leaching of active phase can lead to both catalyst deactivation and the presence of undesired homogenous contribution of condensation reactions. Chemical analysis (ICP) of Al^{3+}, Mg^{2+}, Zr^{4+} and Ca^{2+} in the reaction media after reaction reveals that Mg–Al oxide is most stable to lixiviation: about 0.2% of Mg and Al were lixiviated to the liquid during the reaction. In the case of Mg–Zr mixed oxide, the 2% of the Mg solid content was detected in the aqueous phase, whereas Zr is not present in the reaction medium. The pH was also measured before and after reaction. No significant differences were observed in any case: changes from 10.2 to 10.6 in the reaction with Mg–Zr oxide, and from 8.50 to 9.20 in the Mg–Al case; finally, for Ca–Zr, the pH remained constant in 10.9.

The relevance of this lixiviation – as homogeneously catalyzed reactions – detected during the reaction was evaluated for the most active catalyst (Mg–Zr oxide). In this way, after a condensation reaction, the reaction medium was filtered, compositions of acetone and furfural adjusted to the initial values, and the evolution of the concentrations followed with the time. In a separate experiment, the catalyst was leached with distilled water for 10 h at reaction temperature, being then filtered and using this water as solvent for reaction between acetone and furfural. In both cases, a very scarce homogeneous reaction was detected: conversion of 3–4% of limiting reactant, whereas in presence of catalyst, the conversion at these conditions was close to 80%. Thus, contribution of homogeneous reactions has been discarded in following discussions.

Deactivation studies were carried out with Mg–Al and Mg–Zr oxides (Table 2). Ca–Zr was not tested because of its poor performance in the first reaction. For this purpose, after 24 on stream, catalyst was recovered by filtration, and a new experiment was launched at the same reaction conditions. Although the reactant conversions remain nearly unaltered, selectivity to C13 adduct decreases dramatically after 24 h of reaction. This decrease is more notorious for the Mg–Zr oxide, and can be justified by the modification of either the distribution of basic site or the morphology of the support, hindering the last condensation steps. At this point, it should be taken into account that the chemical modification of the support at mild reaction conditions is essentially reversible. Therefore, characterization techniques involving the use of vacuum or high temperatures are not applicable for studying these causes.

3.4. Reaction mechanism and kinetic modeling

According to the results summarized in the previous sections, the reaction pathway outlined in Scheme 1 can be proposed. In order to gain further understanding on the reaction mechanisms, and to develop a kinetic model for these reactions, reported data was fitted to different kinetic models. The presence of mass-transfer effects has been discarded by both ensuring that particle size and stirring reaction does not affect obtained results, and also by theoretical considerations for the estimation of mass-transfer effects in slurry reactors. The theoretical approach consisted of a kinetic model derivation considering the liquid–solid mass-transfer and the Thiele modulus-based efficiency factor for internal diffusion, demonstrating that external mass transfer is largely faster than intrinsic reaction kinetic, and the efficiency factor is close to one in the reported experiment [32,33].

The temporal profiles of the concentration of acetone, furfural, C8 and C13 adducts were fitted considering an ideal stirred batch reactor behavior. Therefore, unsteady-state mass balances were developed for the four species, considering the velocities of

Table 3
Kinetic constants (min^{-1}) for the fitting of the experimental results to the proposed kinetic model. Reaction 1: condensation of acetone and furfural yielding C8 units; Reaction 2: condensation of C8 and furfural yielding C13 adduct. Negative numbers refer to reverse reaction.

	k_1	k_2	k_{-1}	k_{-2}	r^2
$MgO–ZrO_2$	0.0021	0.006	0.004	0.076	0.97
$MgO–Al_2O_3$	0.0016	1.27	0.0071	1.54	0.96
$CaO–ZrO_2$	0.0024	0.221	0.007	1.71	0.96

formation and decomposition of each compound. Experimental data was fitted using the Scientist software (Burlich–Stoer approximation).

Considering single power-law kinetic models, C8 formation follows first order dependence on acetone concentration and zero-th order on furfural concentration, whereas C13 formation rates presents first and zero-th reaction orders on C8 and furfural concentrations, respectively. In other words, the reaction rates depend on the concentration of the specie which is able to form the carbanion by α-H abstraction. Kinetic data is summarized in Table 3. The goodness of the model for the predictions of evolution of reactants and C8 concentrations is shown in Fig. 9, whereas the fit is not so good for C13, because of its lower average concentration.

According to the reported parameters, Mg–Zr oxide has the highest values of kinetic constants for aldol reaction and the lowest for retroaldolization (k_{-1} and k_{-2}), which explain their good performance. The C13 formation is much more favored using Mg–Al, but k_1 constant has the lowest value for this catalyst, thus not enough reagents (C8) to form C13 are available. Finally, Ca–Zr favors the retroaldolization (highest values of indirect constants), explaining the poor results obtained.

Considering the reaction mechanism, the basis of any base-catalyzed aldol condensation is the catalysts ability to abstract the α-proton of one of the reagents. This depends on two factors: the basicity of the active site and the acidity of that proton [34]. The reaction pathway for producing C8 from the aldol condensation of furfural with acetone, as depicted in Scheme 2, involves the initial abstraction of the α-proton from acetone, forming a carbanion that consecutively attacks the carbonyl group of the contiguously adsorbed furfural molecule [35]. From this reaction, a β–hydroxyl ketone intermediate is expected to be formed; however, this was never observed among the reaction products under the reaction conditions of this work. Therefore, this unstable intermediate is assumed to rapidly dehydrate, in C8 and water regenerating the active sites on the catalyst surface. In a parallel pathway, the carbanion intermediate formed from acetone might attack a second acetone molecule leading to diacetone alcohol and mesityl oxide. In the same form, C13 is obtained by the initial abstraction of the α-proton from C8, forming a carbanion that consecutively attacks the carbonyl group of another adsorbed furfural molecule.

This mechanism can be represented by the following sequence of elementary steps:

$$ACE + * \leftrightarrow ACE* \quad (5a)$$

$$ACE* + \Diamond \leftrightarrow C^-* + H^+\Diamond \quad (5b)$$

$$FFL + * \leftrightarrow FFL* \quad (5c)$$

$$FFL* + C^-* + H^+\Diamond \leftrightarrow C8* + H_2O* + \Diamond \quad (5d)$$

$$C8* \leftrightarrow C8 + * \quad (5e)$$

$$ACE* + H^+\Diamond + C^-* \leftrightarrow DAA* + * + \Diamond \quad (5f)$$

$$DAA* \leftrightarrow DAA + * \quad (5g)$$

$$C8* + \Diamond \leftrightarrow C8^-* + H^+\Diamond \quad (5h)$$

$$FFL* + C8^-* + H^+\Diamond \leftrightarrow C13* + H_2O* + \Diamond \quad (5i)$$

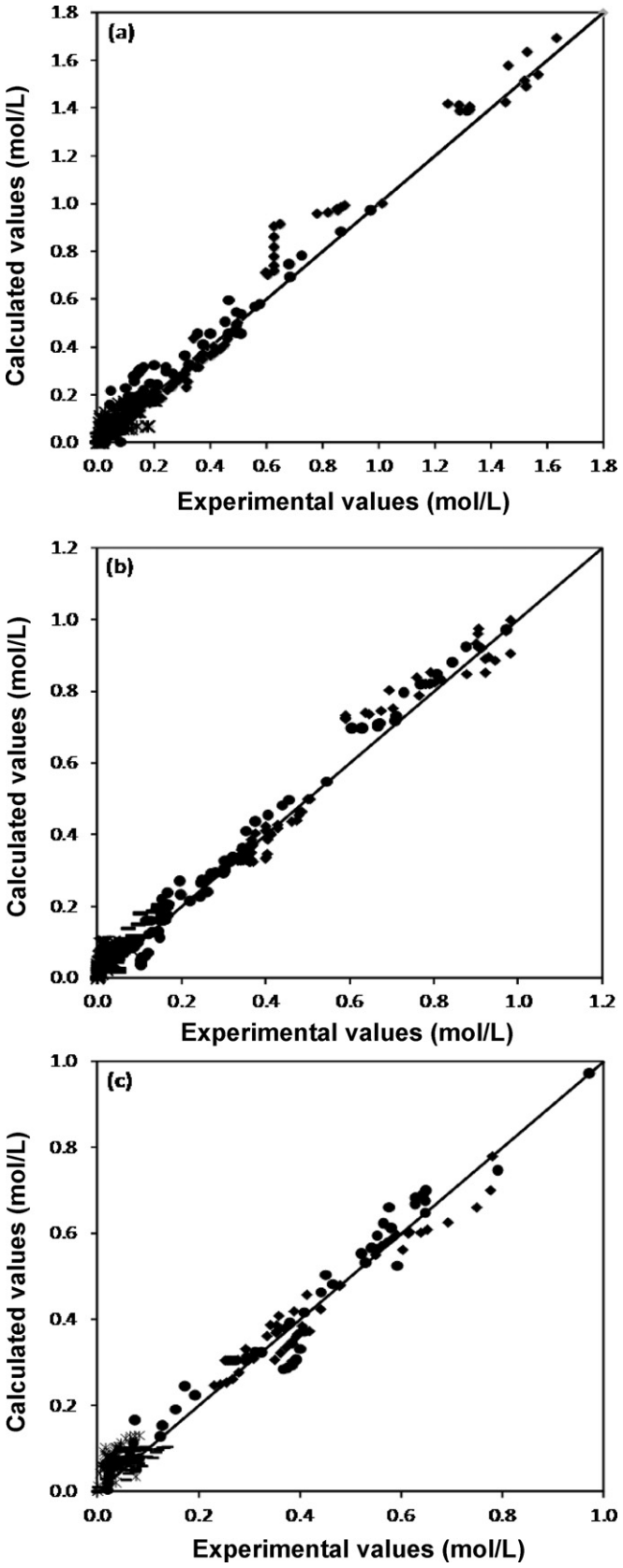

Fig. 9. Summary of the results obtained with the proposed kinetic model in terms of parity plots for the concentration of all the reactants and reaction products for Mg–Zr (a); Mg–Al (b) and Ca–Zr (c). Symbols: C3 (♦); C5 (•), C8 (-); and C13 (*).

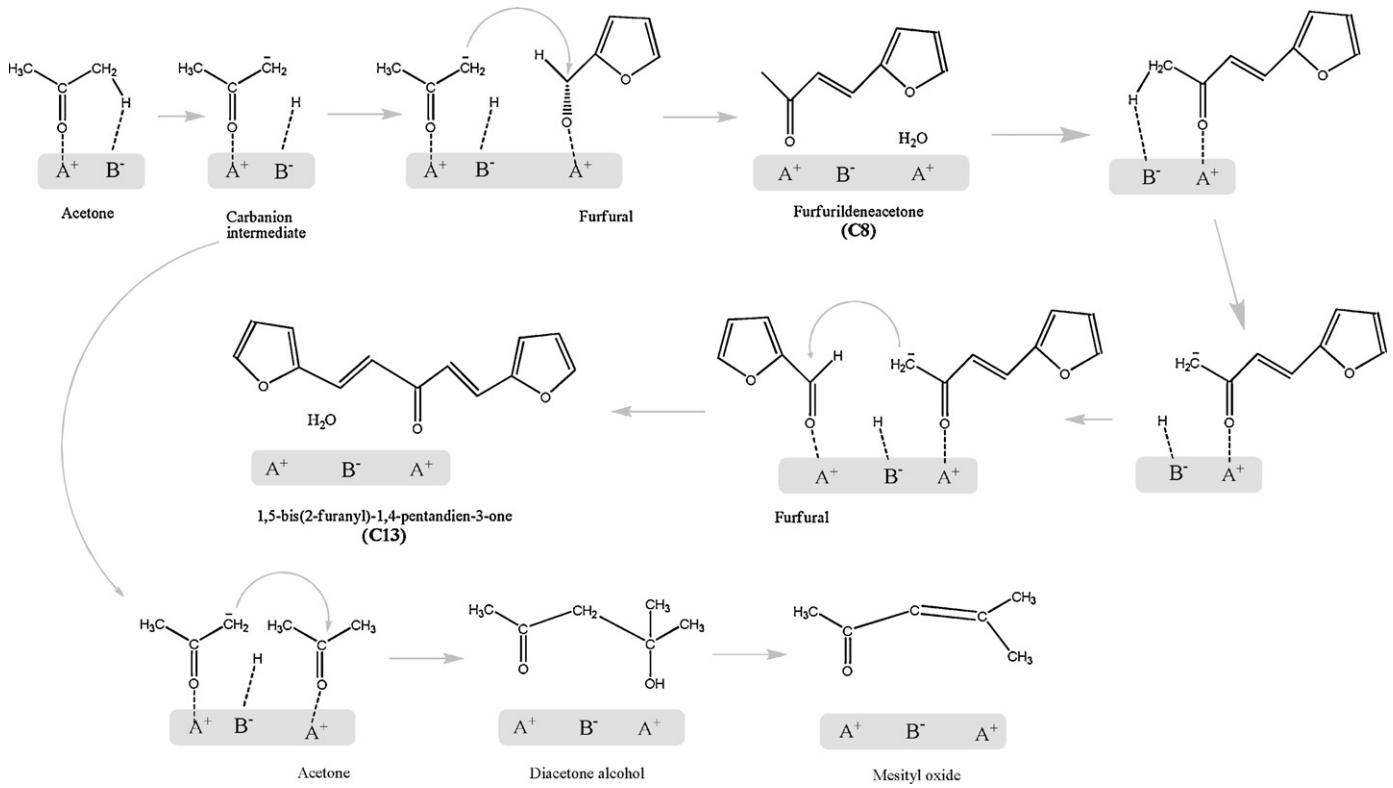

Scheme 2. Surface process for the furfural/acetone aldol condensation.

$$C13* \leftrightarrow C13 + * \quad (5j)$$

$$H_2O* \leftrightarrow H_2O + * \quad (5k)$$

where * represents a metal cation, ◊ an oxygen anion, and C^- is the carbanion formed from acetone. The functions of weak acid sites are to provide an adsorption site for both reagents through their carbonyl groups and to stabilize reaction intermediates.

Based on the proportionality between the initial C8 and diaceton alcohol (DAA) formation rates, the rate-determining step should be shared by both DAA and C8 formation pathways and should involve base sites of a medium strongly basic nature; in the reaction mechanism, that corresponds to step (5b). With the same argument, step (5h) is the rate-determining step to the formation of C13.

4. Conclusions

Three different mixed oxides (Mg–Zr, Mg–Al and Ca–Zr) with basic character have been used as catalysts for aqueous-phase aldol condensation of furfural and acetone. The efficiency of the catalysts decreases in the order Mg–Zr > Mg–Al > Ca–Zr, with the decrease in the concentration of medium-strength basic sites. The concentration of both furfural and acetone also plays a key role in the catalyst performance, being 1:1 molar ratio the most favorable (in spite of the stoichiometric ratio for the formation of the desired C13 adduct is 2:1).

Concerning to the catalyst stability, the fouling effect caused by by-products can be completely neglected, whereas scarce leaching effects have been observed which cause the presence of homogeneous reaction in an extent lower than 4% (versus conversions of 80% were detected for heterogeneous reactor at analogous conditions). Consecutive reaction cycles keep unaltered conversions, although selectivity for C13 formation is decreased.

Finally, a kinetic model has been proposed considering reversible reactions (whose importance has been experimentally demonstrated), first order dependence on the species with available α-hydrogen atoms (species able to form enolates) and zero-th order in the species without these atoms (furfural). This model is congruent with the accepted reaction mechanism.

Acknowledgements

This work was supported by the Spanish Government (contract CTQ2008-06839-C03-02). L. Faba thanks the Government of the Principality of Asturias for a Ph.D. fellowship (Severo Ochoa Program).

Appendix A. Supplementary data

Supplementary data associated with this article can be found, in the online version, at doi:10.1016/j.apcatb.2011.11.039.

References

[1] D.M. Alonso, J.Q. Bond, J.A. Dumesic, Green Chem. 12 (2010) 1493.
[2] S. Zinoviev, f. Müller-Langer, P. Das, N. Bertero, P. Fornasiero, M. Kaltschmitt, G. Centi, S. Miertus, ChemSusChem 3 (2010) 1106.
[3] G.W. Huber, A. Corma, Angew. Chem. Int. Ed. 46 (2007) 7148.
[4] Y. Sun, J. Cheng, Bioresour. Technol. 83 (2002) 1.
[5] R. Xing, A.V. Subrahmayam, H.Olcay, W. Qi, P. van Walsum, G. Pendse, G.W. Huber, Green Chem. 12 (2010) 1933.
[6] M. Käldström, N. Kumar, D.Y. Murzin, Catal. Today 167 (2011) 91.
[7] G.W. Huber, J.A. Dumesic, Catal. Today 111 (2006) 119.
[8] G.W. Huber, J.N. Chheda, C.J. Barret, J.A. Dumesic, Science 308 (2005) 1446.
[9] C.J. Barret, J.N. Chheda, G.W. Huber, J.A. Dumesic, Appl. Catal. B 66 (2006) 111.
[10] R.M. West, Z.Y. Liu, M. Peter, C.A. Gartner, J.A. Dumesic, J. Mol. Catal. A: Chem. 296 (2008) 18.
[11] R.A. van Santen, M. Neurock, Molecular Heterogeneous Catalysis, Wiley, Heidelberg, 2006.
[12] M. Zabeti, W.M.A.W. Daud, M.K. Aroua, Fuel Process. Technol. 91 (2010) 243.
[13] P. Kustrowski, D. Sulkowska, L. Chmielarz, R. Dziembaj, Appl. Catal. A 302 (2006) 317.
[14] K.Y. Foo, B.H. Hameed, Adv. Colloid Interface Sci. 159 (2010) 130.
[15] M. León, E. Díaz, A. Vega, A. Auroux, S. Ordóñez, Appl. Catal. B 102 (2011) 590.
[16] Y. Li, S. Lian, D. Tong, R. Song, W. Yang, Y. Fan, R. Qing, C. Hu, Appl. Energy 88 (2011) 3313.

[17] M.L. Rojas-Cervantes, L. Alonso, J. Díaz-Terán, A.J. López-Peinado, R.M. Martín-Aranda, V. Gómez-Serrano, Carbon 42 (2004) 1575.
[18] I. Sádaba, M. Ojeda, R. Mariscal, J.L.G. Fierro, M.L. Granados, Appl. Catal. B 101 (2011) 638.
[19] M. León, E. Díaz, S. Bennici, A. Vega, S. Ordóñez, A. Auroux, Ind. Eng. Chem. Res. 49 (2010) 3663.
[20] M.A. Aramendía, V. Borau, C. Jiménez, A. Marinas, J.M. Marinas, J.R. Ruiz, F.J. Urbano, J. Mol. Catal. A: Chem. 218 (2004) 81.
[21] L. Faba, E. Diaz, S. Ordóñez, Catal. Today 164 (2011) 451.
[22] S. Liu, J. Ma, L. Guan, J. Li, W. Wei, Y. Sun, Microporous Mesoporous Mater. 117 (2009) 466.
[23] C. Jaques, J. Electron. Spectrosc. 178–179 (2010) 357.
[24] V. Grover, R. Shukla, A.K. Tyagi, Scr. Mater. 57 (2007) 699.
[25] D. Gulková, O. Solcová, M. Zdražil, Microporous Mesoporous Mater. 76 (2004) 137.
[26] J.I. Di Cosimo, A. Acosta, C.R. Apesteguía, J. Mol. Catal. A: Chem. 234 (2005) 111.
[27] G. Wu, S. Jiang, L. Li, N. Guan, Appl. Catal. A 391 (2011) 225.
[28] V. Fournier, P. Marcus, I. Olefjord, Surf. Interface Anal. 34 (2002) 494.
[29] E. Díaz, E. Muñoz, A. Vega, S. Ordóñez, Ind. Eng. Chem. Res. 47 (2008) 212.
[30] F. Arena, R. Dario, A. Parmaliana, Appl. Catal. A 170 (1998) 127.
[31] P. Kustrowski, D. Sulkowska, L. Chmielarz, A. Rafalska-Lasocha, B. Dudek, R. Dziembaj, Microporous Mesoporous Mater. 78 (2005) 11.
[32] H.S. Fogler, M.N. Gürmen, Elements of Chemical Reaction Engineering, 4 ed., Pearson, 2008, ch. 11.
[33] S. Ordóñez, B.P. Vivas, F.V. Díez, Appl. Catal. B 95 (2010) 288.
[34] V.K. Díez, C.R. Apesteguía, J.I. Di Cosimo, J. Catal. 240 (2006) 235.
[35] S. Abelló, F. Medina, D. Tichit, J. Pérez-Ramírez, J.E. Sueiras, P. Salagre, Y. Cesteros, Appl. Catal. B70 (2007) 577.